

# Rational Design Strategy for Triboelectric Nanogenerators Based on Electron Back Flow and Ionic Defects: The Case of Polytetrafluoroethylene

Giulio Fatti,\* Alessandra Ciniero, Hyunseok Ko,\* Han Uk Lee, Yujin Na, Chang Kyu Jeong, Sang-Geul Lee, Dongyub Kwak, Kwi-II Park,\* Sung Beom Cho,\* and Daniele Dini

The lack of theoretical understanding of triboelectrification has hindered the development of energy harvesting technologies like triboelectric nanogenerators. Focusing on polytetrafluoroethylene, a material with a strong triboelectric output, a model predictive of its triboelectric behavior, driving the development of improved nanogenerators are formulated. With a combined computational-experimental approach it is shown that defluorination enhances polytetrafluoroethylene nanoscale triboelectric charging. Then a model, explaining the macroscale triboelectric output as determined by the competition of two mechanisms is developed. Defluorination enhances charging while also reducing the interface gap, favoring the backflow of electrons, and possibly reducing charging. However, numerical analysis shows that backflow is negligible, aligning with the prediction of increased triboelectric output. By building triboelectric nanogenerators with defluorinated polytetrafluoroethylene samples, achieved by X-ray irradiation, a one-order-of-magnitude output increase is demonstrated. The predictive models, supported by experiments, lead to an improved strategy for designing effective energy harvesting devices and new applicative breakthroughs.

## 1. Introduction

Triboelectrification (TE), the electrostatic charging generated by contact or rubbing, is one of the most widespread and commonplace physical phenomena. And yet this phenomenon, so familiar to be cited in primary school textbooks as a simple way to introduce charging for the first time, is one of the longest-studied and less-understood scientific problems. Investigated since the 18<sup>th</sup> century, the complexity associated with the origin of TE has prevented scientists to move on significantly from a pioneering stage. In fact, while a number of important discoveries have been made, many new observations have contradicted existing models, often adding new elements of complexity to the picture.<sup>[1,2]</sup>

Understanding the mechanism underlying TE has profound technological

G. Fatti, A. Ciniero, D. Dini

Tribology Group

Department of Mechanical Engineering

Imperial College London

London SW7 2BX, UK

E-mail: g.fatti18@imperial.ac.uk

G. Fatti

Center of Materials Digitalization

Korea Institute of Ceramic Engineering and Technology (KICET)

Jinju, Gyeongsangnam-do 52851, Republic of Korea

H. Ko

Materials Digitalization Center

Korea Institute of Ceramic Engineering and Technology (KICET)

Jinju, Gyeongsangnam-do 52851, Republic of Korea

E-mail: hko@kicet.re.kr

H. U. Lee, S. B. Cho

Department of Energy Systems Research

Ajou University

Suwon, Gyeonggi-do 16499, Republic of Korea

Y. Na, K.-I. Park

School of Materials Science and Engineering

Kyungpook National University

Daegu 41566, Republic of Korea

E-mail: kipark@knu.ac.kr

C. K. Jeong

Division of Advanced Materials Engineering

Department of Energy Storage/Conversion Engineering of Graduate

School & Hydrogen and Fuel Cell Research Center

Jeonbuk National University

Jeonju, Jeonbuk 54896, Republic of Korea

S.-G. Lee, D. Kwak

Daegu Center

Korea Basic Science Institute

Daegu 41566, Republic of Korea

H. U. Lee, S. B. Cho

Department of Materials Science and Engineering

Ajou University

Suwon, Gyeonggi-do 16499, Republic of Korea

E-mail: csb@ajou.ac.kr

 The ORCID identification number(s) for the author(s) of this article can be found under <https://doi.org/10.1002/aelm.202300333>

© 2023 The Authors. Advanced Electronic Materials published by Wiley-VCH GmbH. This is an open access article under the terms of the Creative Commons Attribution License, which permits use, distribution and reproduction in any medium, provided the original work is properly cited.

DOI: 10.1002/aelm.202300333

implications. Static charges generated from TE are the basis of printing and photocopying<sup>[3]</sup> and of electrospraying;<sup>[4]</sup> they can also cause major issues, such as electrical discharges that damage microelectronic devices<sup>[5]</sup> or disrupt pharmaceutical processes<sup>[6,7]</sup> as well as increased friction and energy losses in industrial processes.<sup>[8,9,10]</sup> Among all the technologies based on TE, the most promising is linked to the development of triboelectric nanogenerators (TENGs).<sup>[11,12,13,14]</sup> TENGs are energy harvesting devices that accumulate tribocharges to provide energy to self-powered sensors,<sup>[15,16,17,18]</sup> portable or wearable devices,<sup>[19,20,21,22]</sup> and a number of other applications.<sup>[18,23,24]</sup> As clean and sustainable sources of energy, TENGs can significantly contribute to the green transition and the Internet of Things.<sup>[13]</sup> Despite the tumultuous growth of the field caused by these recent developments, the approach to optimize the triboelectric output to scale the efficiency up to industrial production has remained mostly heuristic. This has led to significant improvements in controlling the charge output;<sup>[25,26]</sup> however, without a sound theoretical background, these advances have remained at the proof-of-concept stage. Theoretical work has been mainly employed to interpret experimental results, with some success. Especially the recent thermoelectric<sup>[27]</sup> and flexoelectric models<sup>[28,29]</sup> have grasped some fundamental features, explaining how deformation and thermal effects can influence the triboelectric output. Thus far, however, models have yet to achieve the predictive capabilities needed to provide innovative design strategies for scalable engineering solutions. The lack of theoretical understanding has slowed down the development of effective devices that can be successfully employed in real-life applications.

Even regarding polymers, whose triboelectric behavior has been widely studied, researchers have been debating if the underlying mechanism is either related to homolytic or heterolytic ionic transfer or linked to microscopic material transfer.<sup>[5,9,12,30,31]</sup> Other recent studies have pointed out a major contribution from electronic transfer as well.<sup>[32,33]</sup> This uncertainty holds also for the simplest polymers, such as polytetrafluoroethylene (PTFE). PTFE is a linear fluoropolymer (-CF<sub>2</sub>- monomers) and is one of the most tribonegative materials.<sup>[34,35,36]</sup> Because it provides a large triboelectric output, it is widely employed in TENGs' fabrication<sup>[37,38]</sup> and makes an important case study for triboelectrification. In a previous study, we have shown that the large PTFE triboelectricity can only occur when it undergoes defluorination, due to its electronic structure.<sup>[39,40]</sup>

In this article, starting from this finding, we devise a theoretical model to predict how PTFE triboelectric performance can be enhanced by defluorination. After showing that PTFE triboelectric charging grows with increasing defluorination by means of first-principles calculations and corroborating this by Kelvin Probe Force Microscopy (KPFM) measurements,<sup>[41,42]</sup> we show that the macroscopic PTFE triboelectric output is governed by two competing mechanisms. On one hand, charging intensifies because of the increased number of fluorine vacancies acting as electron traps. On the other hand, increased defluorination strengthens the interfacial adhesion, which reduces the interface separation and the interfacial electrostatic barrier. This might reduce triboelectric charging, as it has been shown by the backflow and stuck charges (BSC) model that the barrier prevents the transferred charges from flowing back, determining the

number of "stuck charges" that account for the final triboelectric output.<sup>[43]</sup> We show numerically that in our case the backflow is always negligible, meaning that macroscopic charging should reproduce the microscopic trend. We verify this prediction experimentally both at the micro and at the macroscale, by showing that increased defluorination enhances the triboelectric output of a TENG by an order of magnitude. The theoretical insight gained from the proposed approach and the demonstration of the predictive capabilities it provides will lead to major breakthroughs in several applications of TENGs.

## 2. Results and Discussion

We studied the contact between gold Au(111) and a PTFE chain with increasing defluorination by means of first-principles calculations. The PTFE-Au interface at low and high defluorination is illustrated in Figure 1a, together with a schematic representation of the effect on electronic transfer. Gold was selected because it is triboelectrically neutral,<sup>[35,43]</sup> chemically inert, and its work function is not significantly affected by the surface termination,<sup>[44]</sup> making it especially suitable for experimental testing of triboelectric properties. Au(111) surface was selected because it is gold most stable termination and allows to minimize the lattice mismatch with PTFE. A single PTFE chain was chosen to minimize the configurational complexity, as we showed in a previous study that interchain interactions do not affect PTFE electronic structure.<sup>[39]</sup> We found an Au(111) work function value of 5.15 eV, consistent with previous calculations performed<sup>[44,45]</sup> and in reasonable agreement with the experimental value of 5.35 eV.<sup>[46]</sup> First, we deposited the PTFE chain on gold and studied its more energetically favorable configurations. In general, we found that the system was more stable when fluorine vacancies face the gold surface – see Figure S1.1 (Supporting Information) – as dangling bonds increase PTFE-gold adhesion. Further details about the configurational stability for different defluorination rates are discussed in Experimental section and in Figure S1.2 (Supporting Information).

We then studied the effect of increased defluorination on the PTFE chain triboelectric properties. Figure 1b shows the variation of the interfacial charge density rearrangement, computed as  $\Delta\rho = \rho_{\text{PTFE/Au}} - \rho_{\text{PTFE}} - \rho_{\text{Au}}$ , as the defluorination rate increases. The negative charges (yellow areas) around the chain progressively increase, concentrating around the fluorine vacancies. Figure 1c shows the quantitative evolution of the electronic charges transferred from gold to PTFE as a function of the defluorination rate, calculated through Bader analysis and normalized on the number of monomers in the calculated cell. We found that electronic transfer from gold to PTFE<sup>[47,48]</sup> is negligible for the pristine chain. As the defluorination rate increases, the amount of transferred charge increases more than proportionally. For a fourfold increase of the defluorination rate, we observe that triboelectric charging rises by more than five times. This trend suggests that PTFE triboelectric behavior is governed by homolytic defluorination. Once the C–F bonds are severed, the remaining dangling bonds can capture electrons from the gold counter-surface, i.e., they act as electron traps. However, this trend cannot be verified experimentally because charging is only indirectly accessible at the nanoscale, through the KPFM measurement of the contact potential and work function. Therefore, we calculated the

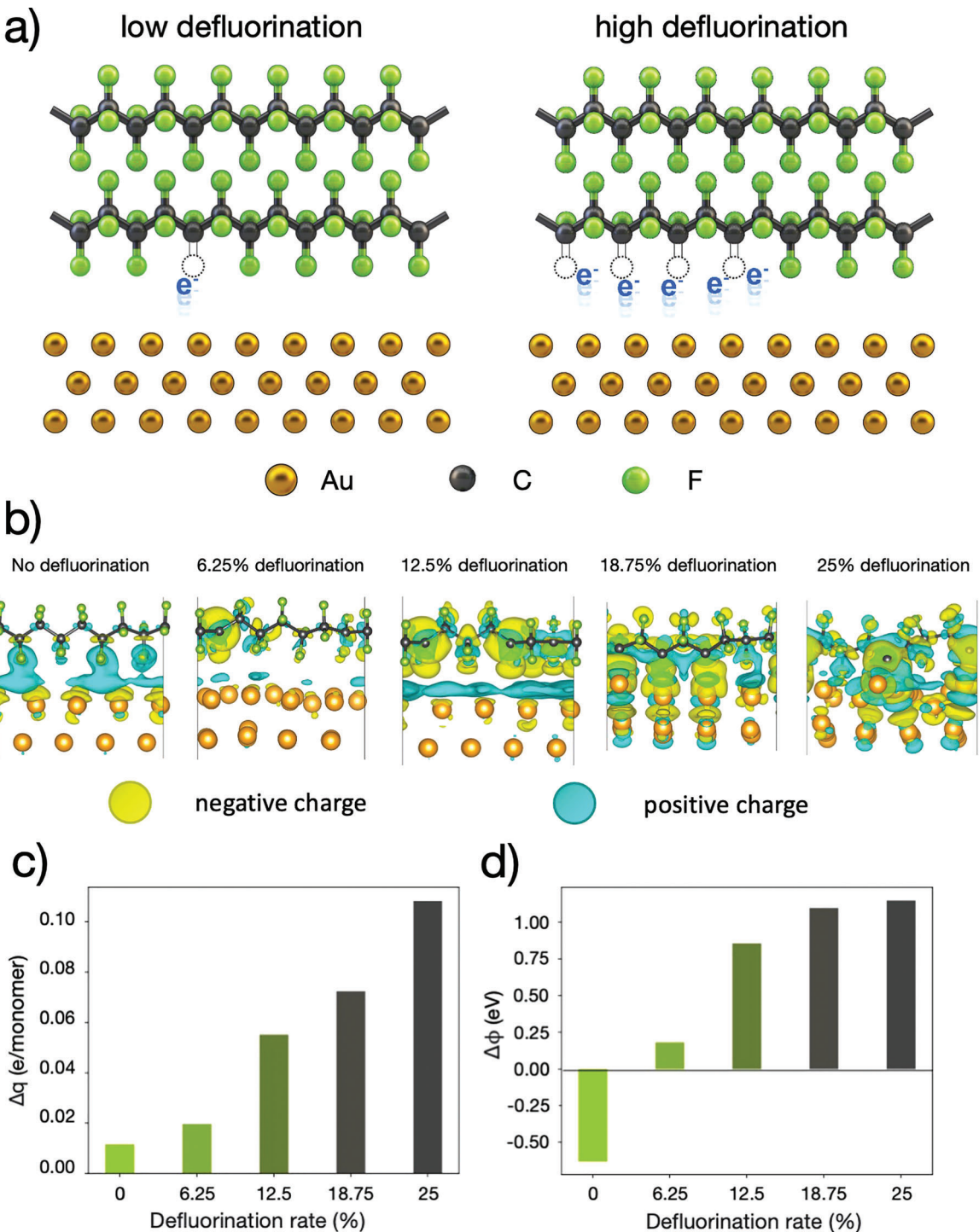


**Figure 1.** a) Illustrative representation of the enhanced charging induced by increased defluorination; b) interfacial charge density rearrangement at the calculated defluorination rates; c) electronic charge transferred from gold to PTFE, normalized on the number of monomers in the PTFE chain, and d) work function change with respect to the pristine Au(111) surface versus the defluorination rate.

work function from first principles, to make a direct comparison with experimental measurements.

Figure 1d shows the calculated work function change that PTFE deposition induces with respect to pristine gold versus defluorination rate, calculated as:  $\Delta\varphi = \varphi - \varphi_0$ , where  $\varphi$  is the

work function of the gold-PTFE system, and  $\varphi_0$  the work function of Au(111). Notably, the deposition of pristine PTFE induces a reduction of the work function to 4.5 eV, in agreement with reports of other fluorinated molecules.<sup>[49]</sup> After the chain is defluorinated, the  $\Delta\varphi$  sign is inverted, which indicates that the work

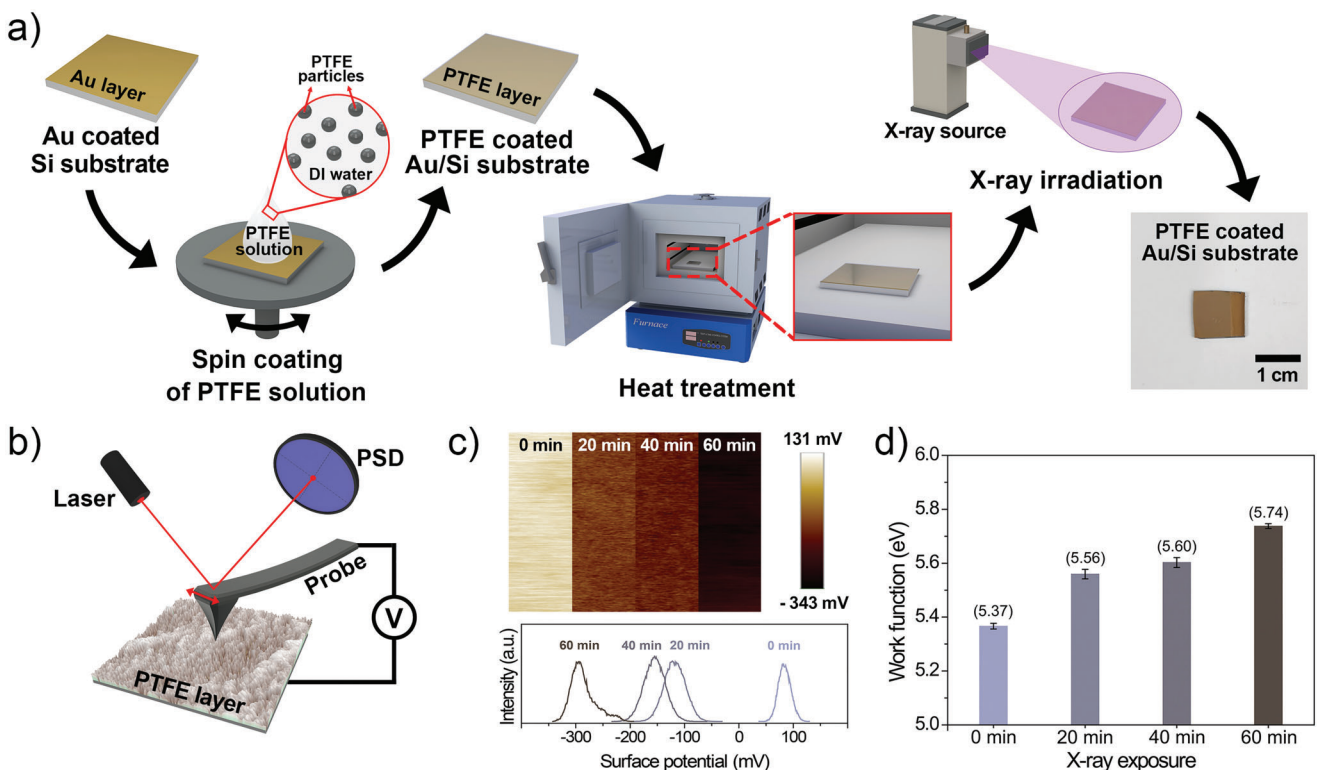


**Figure 2.** a) Schematic diagram for the deposition of PTFE onto Au/Si substrates and X-ray irradiation process; b) schematic illustration for the KPFM analysis of the PTFE layer coated an Au/Si substrate; c) the measured surface potential images (top) and distribution curves (bottom) of PTFE layers with X-ray irradiation process; d) work function measurement results of the samples as a function of the time of exposure to X-rays.

function increases with the defluorination rate, increasing up to 6.25 eV. The trend is not exactly proportional to the calculated charge transfer because the work function is proportional to the surface dipole rather than to the surface charge density, meaning that it is sensitive to local charge density rearrangements.<sup>[50,51,52]</sup> Nonetheless, the trend is coherent with the increasing electron transfer, which, significantly, allows for the experimental verification of our theoretical findings.

Previous reports have shown that PTFE can be defluorinated using several methods, including X-rays irradiation<sup>[53]</sup> and exposition to sodium,<sup>[54]</sup> potassium<sup>[55]</sup> and hydrogen plasma.<sup>[56]</sup> Among them, the irradiation of PTFE by X-rays is the most suitable method because it does not affect its chemical composition. This ensures that the experimental conditions reproduce the calculations set-up in the most accurate way. **Figure 2a** shows a schematic illustration of the deposition procedure of a PTFE layer on an Au/Si substrate. After the deposition of PTFE on gold, using the technique described in the Methods section, we irradiated it with X-rays at 1.2 kW for 20, 40, and 60 min. To directly investigate the work function of X-ray-irradiated PTFE, we measured the contact potential difference (CPD,  $V_{CPD}$ ) between a conductive Pt/Ir coated KPFM tip and the PTFE sample, as shown in the diagram in **Figure 2b**. The work function of the PTFE samples can be calculated from the relation  $\varphi_{sample} = \varphi_{tip} - eV_{CPD}$ , where  $\varphi_{sample}$  is the work function of PTFE deposited on gold,  $\varphi_{tip}$  is the work function of the Pt/Ir coated tip, and  $e$  is the electronic charge. The sample preparation and the detailed procedure of the KPFM analysis is provided in the Methods section. **Figure 2c**

shows the surface potential difference (top panel) and the distribution curves (bottom panel) between a probe and the X-ray irradiated PTFE layers with different exposure times.

To guarantee the reproducibility of the measured data, we performed five KPFM analyses at different positions on the PTFE sample. **Figure 2d** shows the measured average work function – and the relative error bars – of the gold-PTFE system against the time of exposure to X-rays. Table S2 in the Supporting Information presents the measured work function values of the irradiated PTFE layers from which the mean values and error bars were computed. Like in our calculations, the measured work function monotonically grows with a longer X-ray irradiation time, showing an upward trend that is an unmistakable sign of increasingly negative triboelectric output. These results correlate remarkably well with the calculated work function values, which span from 4.5 eV with no defluorination to 6.25 eV with a 25% defluorination rate. To confirm that the effect is governed by defluorination, we investigated the samples by X-ray photoelectron spectroscopy analysis, as shown in Figure S3 (Supporting Information). The C1s and F1s peaks, relative to organic carbon and fluorine, both decrease with increasing X-ray irradiation time, demonstrating the decrease in fluorine content caused by X-rays exposure.

At this point, we designed a theoretical model to predict PTFE triboelectric behavior at the macroscale, starting from the results obtained from the calculations. First, we tested our findings against the BSC model that has proved to accurately predict the triboelectric output of dielectrics at the macroscale.<sup>[43]</sup> This will allow us to bridge the gap between the atomistic scale of the

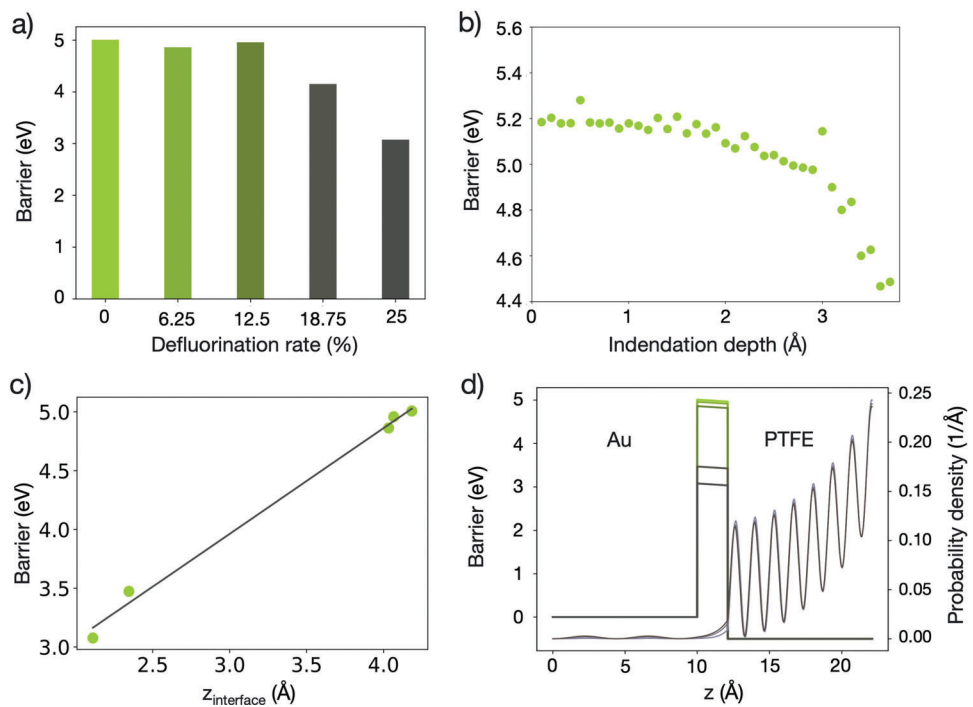


**Figure 3.** a) Electrostatic barrier versus defluorination rate; b) decrease of the electrostatic barrier during the indentation of defluorinated PTFE (6.25%) toward gold; c) electrostatic barriers shown in a) against their respective interface separation (blue circles) and linear fit (black line); d) numerical estimation of the backflow probability for the considered barriers.

calculations and the macroscale of the applications, showing that our theoretical results can also be employed to effectively enhance the triboelectric output of real devices. According to the BSC model, a positive correlation exists between electronic transfer and the electrostatic barrier at the interface. First, mechanical stresses allow electrons to cross the barrier in the approaching stage of contact. When stress is relieved during separation, the barrier prevents the transferred electron from flowing back and increases the number of “stuck charges” that eventually determine the triboelectric output. According to this mechanism, one would expect the electrostatic barrier to increase at larger defluorination rates, in agreement with the electron transfer trend (Figure 1a). Figure 3a shows instead that the calculated electrostatic barrier actually falls as the defluorination rate grows. This finding seems to critically contradict the BSC model when bond ruptures are involved. In fact, we are going to show that this behavior depends on a more complex dual mechanism, that involves an increase of charging due to the higher number of defect states, and a competing decrease of charging caused by a larger backflow due to a lower barrier.

In the first instance, we found that the electrostatic barrier height depends on the interface separation. Using a quasi-static first principles procedure devised for the study of mechanochemical reactions,<sup>[57]</sup> we investigated the approaching stage of contact, when PTFE and gold are pushed into contact by mechanical stresses. In this procedure, PTFE and gold are initially set at a fixed distance, larger than the equilibrium separation to simulate a real approaching situation, and the configuration is statistically optimized. Then PTFE is moved closer to gold by 0.1 Å, the distance is fixed, and the system is relaxed again. This in-

dentation procedure is iterated until the interface separation is smaller than the equilibrium distance. A chain with one fluorine vacancy – a 6.25% defluorination rate – was employed for the calculations as a model case. Further details on the indentation can be found in the Methods section. Figure 3b shows the barrier dependence on the indentation. The electrostatic barrier decreases slowly until PTFE reaches the equilibrium distance, at  $\approx 2.5$  Å indentation depth. From this point, the two materials are pushed into the region of repulsive forces and the barrier starts to decrease much faster. This supports the assumption made by the BSC model that the forward flow of electrons is activated by mechanical forces, because a lower barrier should facilitate the electron transfer in the approaching stage. Moreover, this trend clearly shows that the barrier is not just material-determined but also a function of the interface separation.

This dependence is key to understanding why the electrostatic barrier goes down with increasing defluorination, despite the significant growth of the transferred charge. Figure 3c shows the same electrostatic barriers represented in Figure 3a, against their respective interface separations. It can be clearly observed that the barrier is a linear function of the interface separation, as highlighted by the linear fit (black line). This is because the defluorination also affects the equilibrium interface distance. A growing number of dangling bonds at the interface strengthens the interfacial adhesion and draws PTFE and gold closer, which in turn lowers the barrier. However, this decrease is not directly related to the increasing triboelectric charging, meaning that the explanation provided by the BSC model still holds when the surfaces are separated.

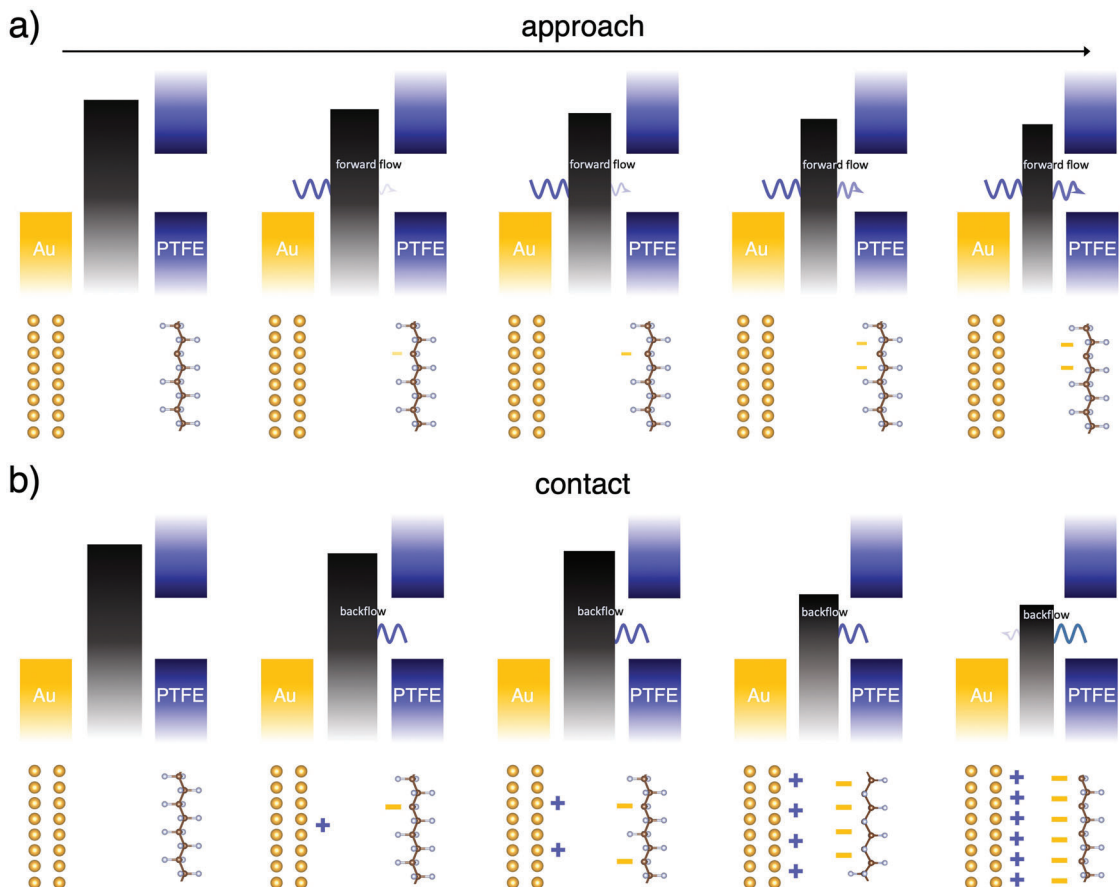


**Figure 4.** Schematics of the refined BSC model. a) Approaching stage: as PTFE and gold are pushed closer by mechanical forces, the electrostatic barrier gets lower and enables the forward flow of electron; b) Contact stage: charging is governed by the competition between the larger electron transfer prompted by an increasing defluorination and a larger backflow, due to the lower barrier caused by a smaller interface separation.

Although this resolves the apparent contradiction between our calculations and the BSC model, a lower barrier at a higher defluorination rate might nonetheless cause a decreased macroscopic triboelectric output with respect to the calculated values. DFT calculations, which are performed at equilibrium conditions, cannot “see” the electron backflow occurring during separation, but in principle, a lower barrier might cause a higher electron backflow. This would result in a lower macroscale triboelectric output with respect to the calculated one. In this case, however, a numerical calculation of the tunneling probability across the different calculated barriers shows that, when an electron is located on the PTFE surface, it has a very slight probability of flowing back to the gold countersurface. Figure 3d shows that the probability density of the electron wave function remains almost entirely on PTFE, with only a slight probability of tunneling back to the gold countersurface. Even for the lowest barrier and the shortest interface separation, the backflow probability is not larger than 1%, meaning that the electron backflow does not contribute significantly to reduce the triboelectric charging in this specific system.

Therefore, when homolytic defluorination is included in the picture, the triboelectrification mechanism can be described as the result of a complex dynamics, involving different and competing mechanisms. We schematically summarize this in a more general version of the BSC model, as shown in Figure 4. First,

during approach (Figure 4a), the two surfaces are drawn into contact by mechanical forces and the electrostatic barrier, decreasing, facilitates the initial transfer, or the forward flow of electrons. It is important to note that contact forces can be extremely high at the nanoscale,<sup>[58,59]</sup> meaning that the interface separation reduces below the equilibrium distance at this stage. It is during this stage that charges can be transferred across the interface, facilitated by a lowering barrier, as already shown in Figure 3b. The forward flow of charge can be larger or smaller depending on the defluorination rate, which is proportional to the number of electron trap states on PTFE.

Then, when stress is released and surfaces relax at their equilibrium distance, the final triboelectric output is determined by the competition between two mechanisms, as shown in Figure 4b. On one hand, an increasing defluorination implies more dangling bonds at the interface acting as electron traps, prompting a larger electron transfer. On the other hand, defluorination also increases the interfacial adhesion, because the uncoupled electrons on the dangling bonds bind more strongly to gold. This narrows the interface separation and reduces the barrier proportionally. However, this does not affect the backflow intensity, as our numerical calculations show that the barrier is always high enough to prevent the backflow almost entirely. Our model thus predicts that defluorination would induce a

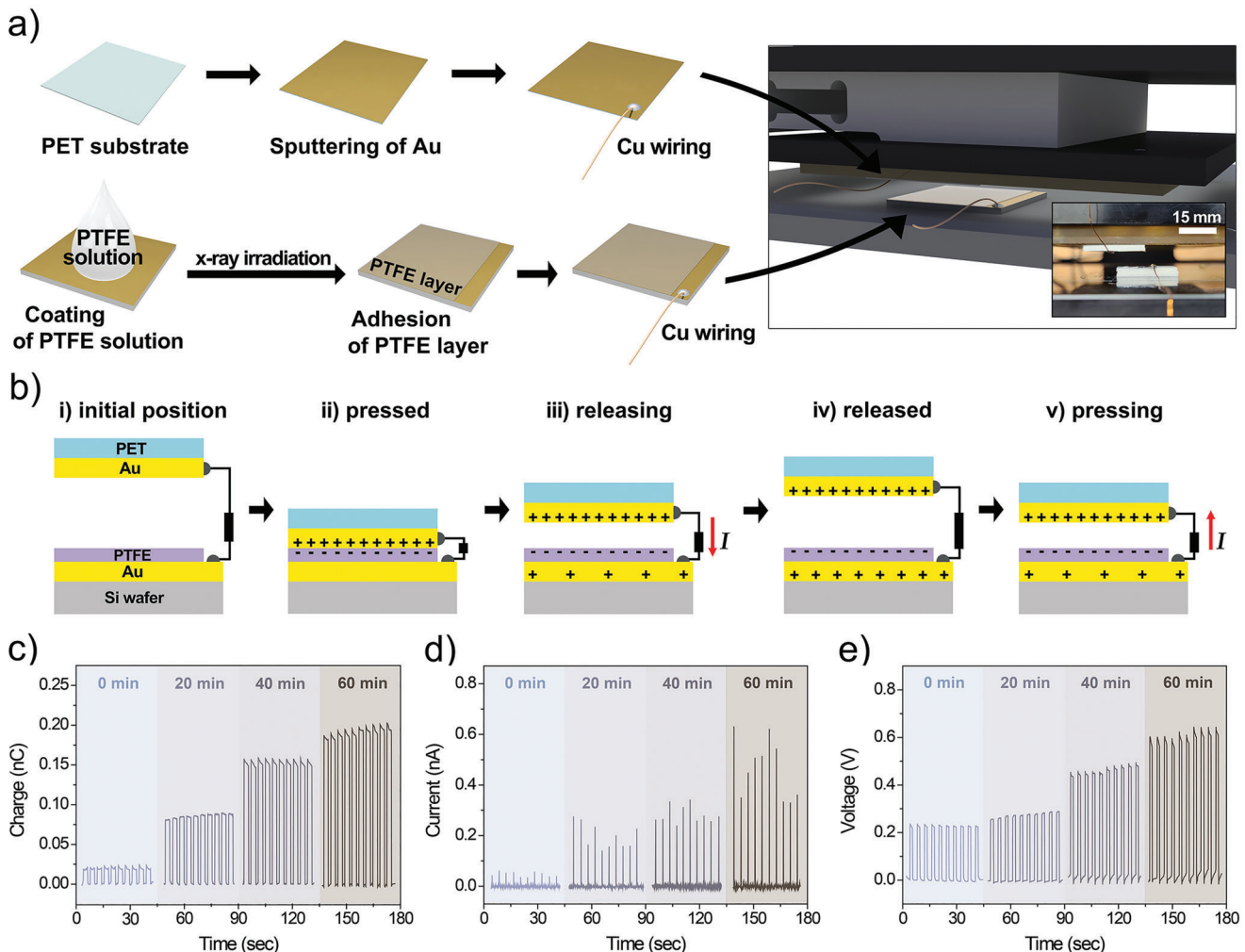


**Figure 5.** a) Schematic of the preparation of a PTFE-based structure to characterize the triboelectric output of the X-ray irradiated samples. The right panel and the inset show, respectively, the schematics and photograph of the vertical CS mode setup for measuring the triboelectricity; b) Diagram of the pushing/releasing mechanism to generate the triboelectric signal; c–e) triboelectric output signals of PTFE measured by means of the CS mode triboelectric device as a function of the time of exposure to X-ray irradiation; c) Charge, d) current, and e) voltage output versus exposure times.

progressive increase of the triboelectric output also at the macroscopic scale, at least up to the highest considered defluorination rate (25%).

To verify our prediction experimentally, we analyzed the harvested output signals from PTFE on a triboelectric nanogenerator device, whose preparation and design are illustrated in Figure 5a, employed in a contact-separation (CS) mode (right panel of Figure 5a). The sample preparation and measurement procedure are described in detail in the Method section. Figure 5b describes a full cycle of the triboelectricity-generating mechanism for the vertical CS mode. At the initial position (Figure 5b-i), the PTFE and gold (Au) surfaces are distant, and there is no induced charge, and therefore there is no electrical potential difference between the PTFE and Au layers either. When the surfaces are brought into contact by external forces (Figure 5b-ii), triboelectrification takes place and electrons flow from Au to PTFE, which gains net positive and net negative charges, respectively. After charging, the surfaces are separated and a potential differ-

ence between them is established (Figure 5b-iii). This, in turn, induces an external current flow ( $I$ ) from Au to PTFE to balance the potential difference. As the surfaces reach the completely released state, the current progressively drops to zero because it neutralizes the charges. Finally, Au and PTFE are pushed toward each other once again, the potential difference decreases and the current starts flowing in the opposite direction (Figure 5b-v). As a result, an alternating signal is obtained by reiterating pressing and releasing.<sup>[60,61,62]</sup> The CS mode involves only vertical contact and separation, which allowed us to avoid more complicated processes with shear stresses and wear.<sup>[63,64,65]</sup> We characterized the triboelectric output generated during the pushing/releasing motion employing PTFE samples irradiated for the same times of exposure as in Figure 2, realizing a different device for each different time. Figure 5c–e shows the measured charge, short-circuit current, and open-circuit voltage, respectively, as a function of the time of exposure to X-rays. These results show that the triboelectric output grows significantly as the exposure time

to X-rays increases. Looking more closely at the trend we see that, before PTFE is exposed to X-rays, the measured triboelectric output signal is very close to zero, like in the first principles calculations. As the exposure time increases, triboelectrification grows in intensity more than linearly, with a proportionality that closely matches the theoretical results. X-ray exposure tends to slightly increase the surface roughness, as shown in Figure S4 (Supporting Information). The increase is very slight, which should only marginally reduce the area available for contact. In any case, a reduced area of contact should reduce the number of charges that can be transferred, the effect caused by defluorination is clearly strong enough to compensate for the increased roughness. Moreover, it suggests that a treatment to reduce the surface roughness could further increase the triboelectric output.<sup>[66,67,68]</sup> Additionally, we characterized the triboelectric output signals by contact between our triboelectric generator and polyethylene terephthalate (PET) substrate (Figure S5, Supporting Information). This shows that the enhancement of the triboelectric output is independent of the surface in contact with PTFE and can be generalized to both polymer-polymer and polymer-metal contact. These results strongly support our theoretical prediction, showing that a deeper theoretical understanding is crucial to provide insights for improving the development of applications.

### 3. Conclusion

In this work, we successfully devised a theoretical model that allows to predict the macroscopic PTFE triboelectric behavior starting from first principles calculations. Analyzing the calculations, we showed that PTFE triboelectric charging is governed by homolytic defluorination. Studying contact between PTFE and gold, we found that a growing defluorination rate intensified the electronic transfer from gold to PTFE. At the same time, the calculated work function increased monotonically as well, which allowed for the experimental verification of these results by KPFM measurements on PTFE samples defluorinated by X-rays. We employed the BSC model to predict the macroscopic triboelectric charging from the first principles results. We generalized the model, showing that the final triboelectric output is determined by the competition of two mechanisms, an increased triboelectric charging due to larger defluorination versus a lower electrostatic barrier, due to a narrower interface separation caused by a larger adhesion. This in turn should prompt a larger electron backflow, that would reduce the stuck charges and ultimately the macroscopic charging. A numerical simulation of the backflow probability, however, showed that the backflow probability is very low for our specific system. With a negligible backflow, we theoretically predicted that defluorination would enhance triboelectric charging also at the macroscale, which was confirmed by triboelectric measurements with remarkable accuracy. The consistency of the triboelectric measurements for contact with very different materials, such as gold and PET, proves that the results are general and independent of the countersurface. Therefore, we proved that our theoretical model is predictive of the macroscopic triboelectric output and can be effectively employed to improve the performances of energy harvesting devices. This shows that a deeper theoretical understanding is crucial to provide insights and a consistent strategy for bettering the design and development of scalable engineering solutions in this area.

### 4. Experimental Section

**Computational Details:** The triboelectric properties of defluorinated PTFE in contact with gold were studied by means of plane-wave DFT calculations using the Quantum Espresso (QE) package.<sup>[69]</sup> The exchange-correlation potential was described by the Perdew-Burke-Ernzerhof (PBE) functional,<sup>[70]</sup> corrected by a dispersion term to model the long-range van der Waals interactions, modeled according to the semiempirical method by Grimme (DFT-D2).<sup>[71]</sup> The ionic species were described by ultrasoft pseudopotentials, and a kinetic cutoff of 35 (280) Ry was employed to truncate the wave function (charge density) expansion. The calculated gold lattice constant  $a_{\text{Au}} = 4.21 \text{ \AA}$  was only slightly larger than the experimental value  $a_{\text{exp}} = 4.08 \text{ \AA}$ ,<sup>[72]</sup> which was a well-known feature of the PBE functional. The calculated PTFE monomer length was  $x_{\text{PTFE}} = 2.65 \text{ \AA}$ , also in good agreement with the experimental value  $x_{\text{exp}} = 2.62 \text{ \AA}$ .<sup>[73]</sup> Au(111) termination was chosen because it was the most stable gold surface. A gold  $3\sqrt{3} \times 4$  supercell was employed to minimize the lattice mismatch at 2.5%, aligning the PTFE chain along the  $y$  axis. The Brillouin zone was sampled by a  $3 \times 1 \times 1$  Monkhorst-Pack grid,<sup>[74]</sup> and a gaussian broadening with a 0.005 smearing width was used to calculate the fractional occupancies.

**Work Function and Interfacial Electrostatic Barrier:** The work function was calculated as:

$$\varphi = E_V - E_F \quad (1)$$

where  $E_F$  was the calculated Fermi level and  $E_V$  was the electrostatic potential calculated in the vacuum region of the cell by the post processing package provided in Quantum Espresso. The electrostatic barrier was the quantity governing electron transfer at the interface, and can be calculated from first principles as well, as:

$$W_b = E_m - E_F \quad (2)$$

where  $W_b$  was the barrier and  $E_m$  was the maximum electrostatic potential at the interface and  $E_F$  the Fermi level.

**First Principles Indentation Procedure:** At the beginning of the indentation, PTFE and gold were set at a fixed interface separation of 5 Å distance between the PTFE carbon backbone and the gold surface layer. Then the separation was progressively reduced by quasi-statically indenting the PTFE chain by 0.1 Å steps toward gold, iterating until the interface separation becomes shorter than the equilibrium distance, for forty steps. At every step, the system was relaxed again by keeping fixed the external fluorine atoms and the bottom gold layer, so that the interface separation was carefully controlled, while the rest of the system was allowed to relax.

**Numerical Analysis of the Backflow Probability:** The backflow probability was calculated as the probability that an electron on the PTFE surface tunnel the interface electrostatic barrier and flow back to gold. The Schrödinger equation for a 1D quantum barrier was:

$$\hbar^2 \nabla \cdot \left( \frac{\nabla \psi(x)}{2m_{\text{eff}}(x)} \right) + V(x) \psi(x) = E \psi(x) \quad (3)$$

where  $m_{\text{eff}}$  was the effective mass,  $\hbar$  was the Planck constant,  $E$  was the total energy and  $V(x)$  was the potential energy, which was set as:

$$V(x) = 0, \quad x < 0 \quad (4)$$

$$V(x) = W_b - \frac{\sigma}{\varepsilon_0} x, \quad 0 < x < x_{\text{bar}} \quad (5)$$

$$V(x) = -0.5 \text{ eV}, \quad x > x_{\text{bar}} \quad (6)$$

where  $W_b$  was the barrier height,  $x_{\text{bar}} = 2.1 \text{ \AA}$  was the barrier width, corresponding to the shortest calculated interface distance, and the term

$-\frac{\sigma}{\epsilon_0}x$  was included to take into account the electrostatic potential difference established across the interface after charge transfer. In this term,  $\sigma$  was the surface charge density and  $\epsilon_0$  was the vacuum permittivity. The Fermi level was set as the reference energy at 0 eV. The model considers gold at  $x < 0$  and PTFE at  $x > x_{\text{bar}}$ , where the potential was lower than zero because the states where electrons were captured have an energy lower than the Fermi level. The  $m_{\text{eff}}$  of gold and PTFE was set as  $m_{\text{eff},\text{Au}} = 1.1 m_e$  and  $m_{\text{eff},\text{PTFE}} = 9.0 m_e$ , respectively, where  $m_e$  was the electron mass. The equation was numerical solved using COMSOL Multiphysics.<sup>[75]</sup>

**Deposition and X-Ray Irradiation of PTFE Layer.** A 30 wt% PTFE aqueous dispersion, which was made with DI water and 60 wt% PTFE dispersion (SFN-2H, Zhonghao Chengguang Research Institute of Chemical Industry Co., Ltd.), was spin-casted on an Au coated Si substrate with the size of  $1 \times 1 \text{ cm}^2$  by spin coater (ACE-200, Dong Ah Trade Corp.) at 5000 rpm for 30 s. The dispersed PTFE solution on Au/Si wafer was dried in a convection oven at 100 °C for an hour. Then, heat treatment was carried out in a furnace at 350 °C for two hours to make the PTFE layer crystalline and reduce the stresses on it.<sup>[76]</sup> The Au/Si substrate coated by the PTFE layer was irradiated by X-ray using a multi-purpose X-ray diffractometer (MP-XRD, X'PERT PRO MRD, Philips, Netherlands) with a Cu K $\alpha$  radiation source ( $\lambda = 1.54184 \text{ \AA}$ ). The X-ray irradiation was operated at a power of 1.2 kW (tension of 40 kV and current of 30 mA) and at an incident angle 15° for 0, 20, 40, and 60 min.

**KPFM Analysis of X-Ray Irradiated PTFE Layer.** The surface potential and work function of each PTFE deposited Au/Si substrate were characterized by a KPFM analysis of atomic force microscopy (AFM, NX20, Park Systems, South Korea) with a PtIr<sub>5</sub>-coated conductive probe (PPP-EFM, Nanosensors, Switzerland). A bias of 2 V was applied to the conductive tip at the surface of the PTFE layers. The surface potential values of PTFE layers was investigated on each sample by KPFM analysis and computed the work function of them by the following equation:

$$V_{\text{CPD}} = \frac{\varphi_{\text{tip}} - \varphi_{\text{sample}}}{e} \quad (7)$$

which holds when the bias was applied to the tip.<sup>[77,78]</sup>  $V_{\text{CPD}}$  was defined as the contact potential difference, and it has the same value as the surface potential. A value of 5.45 eV was putted as the work function of the PtIr<sub>5</sub>-coated tip ( $\varphi_{\text{tip}}$ ) based on Ref. [79] At each exposure time, 5 measurements was taken, shown in Table S2 in the Supporting Information. The error on the measurements was calculated as the standard deviation of these measurements.

**Characterization of the Triboelectric Output of the X-Ray Irradiated 81PTFE Layers.** To evaluate the triboelectric performance of PTFE layers with different X-ray exposure times, PTFE deposited devices with the size of  $1.5 \times 1.5 \text{ cm}^2$  was fabricated through the same fabrication procedure employed on the samples for KPFM measurement. Additionally, Cu wires were attached to the Au electrode of PTFE device using conductive epoxy. As a counter-surface, a  $1.2 \times 1.5 \text{ cm}^2$  sized Au layer was prepared, which acts as the tribopositive layer. The Au deposition layer was formed onto a PET substrate by sputtering process and a copper wire was fixed to this electrode as well. The surface of the gold electrode using polydimethylsiloxane (PDMS) was encapsulated to cover the protrusion of the epoxy (right panel and inset in Figure 5a). The cyclic pushing/releasing motion was performed by a pushing machine (Pushing Machine System, SnM) with an external load of  $\approx 18 \text{ N}$ . The applied load was estimated using a load cell (BCA-10L, CAS) and monitored using a weighing indicator (NT-505A, CAS). The triboelectric output, such as the converted charge, short-circuit current, and open-circuit voltage at constant pressure were measured using an electrometer (6514 System electrometer, Keithley) and recorded on a pushing system program in real-time.

## Supporting Information

Supporting Information is available from the Wiley Online Library or from the author.

## Acknowledgements

This research was supported by National R&D Program through the National Research Foundation of Korea (NRF) funded by Ministry of Science and ICT (2021R1A4A2001658, 2022R1A2C1003853, 2022R1F1A1063060 and RS-2023-00209910) and by the Virtual Engineering Platform Project through the Ministry of Trade, Industry, and Energy of Korea (P0022336). The computational resource was partially supported by Korea Supercomputing Center (KSC-2022-CRE-0352).

## Conflict of Interest

The authors declare no conflict of interest.

## Data Availability Statement

The data that support the findings of this study are available from the corresponding author upon reasonable request.

## Keywords

DFT calculations, energy harvesting, polytetrafluoroethylene, triboelectrification, triboelectric nanogenerators

Received: May 18, 2023

Revised: August 1, 2023

Published online: September 8, 2023

- [1] D. J. Lacks, *Angew. Chem. Int. Ed.* **2012**, *51*, 6822.
- [2] D. J. Lacks, T. Shinbrot, *Nat. Rev. Chem.* **2019**, *3*, 465.
- [3] D. M. Pai, B. E. Springett, *Rev. Mod. Phys.* **1993**, *65*, 163.
- [4] A. Jaworek, A. T. Sobczyk, *J. Electrostat.* **2008**, *66*, 197.
- [5] H. Tarik Baytekin, B. Baytekin, T. M. Hermans, B. Kowalczyk, B. A. Grzybowski, *Science* **2013**, *341*, 1368.
- [6] J. Daniel, *J. Electrost.* **2017**, *87*, 64.
- [7] Y. Pu, M. Mazumder, C. Cooney, *J. Pharm. Sci.* **2009**, *98*, 2412.
- [8] N. Luo, Y. Feng, L. Zhang, W. Sun, D. Wang, X. Sun, F. Zhou, W. Liu, *Nano Energy* **2021**, *87*, 106183.
- [9] T. A. L. Burgo, C. A. Silva, L. B. S. Balestrin, F. Galernbeck, *Sci. Rep.* **2013**, *3*, 2384.
- [10] K. Sayfidinov, S. Doruk Cezan, B. Baytekin, H. Tarik Baytekin, *Sci. Adv.* **2018**, *4*, eaau3808.
- [11] F.-R. Fan, Z.-Q. Tian, Z. L. Wang, *Nano Energy* **2012**, *1*, 328.
- [12] C. K. Jeong, K. M. Baek, S. Niu, T. W. Nam, Y. H. Hur, D. Y. Park, G. T. Hwang, *Nano Lett.* **2014**, *14*, 7031.
- [13] J. Li, C. Wu, I. Dharmasena, X. Ni, Z. Wang, H. Shen, S. L. Huang, W. Ding, *Intell. Converged Netw.* **2020**, *1*, 115.
- [14] S. Beom, *Adv. Mater.* **2020**, *32*, 1905539.
- [15] Z. L. Wang, *ACS Nano* **2013**, *7*, 9533.
- [16] T. Tat, A. Libanori, C. Au, A. Yau, J. Chen, *Biosens. Bioelectron.* **2021**, *171*, 112714.
- [17] Z. L. Wang, J. Chen, L. Lin, *Energy Environ. Sci.* **2015**, *8*, 2250.
- [18] L. Xu, T. Jing, P. Lin, J. J. Shao, C. He, W. Zhong, X. Y. Chen, Z. L. Wang, *ACS Nano* **2018**, *2*, 1849.
- [19] Y. Wang, Y. Yang, Z. L. Wang, *npj Flexible Electron.* **2017**, *1*, 10.
- [20] W. Paosangthong, R. Torah, S. Beeby, *Nano Energy* **2019**, *55*, 402.
- [21] L. Niu, J. Wang, K. Wang, H. Pan, G. Jiang, C. Chen, P. Ma, *Adv. Fiber Mater.* **2023**, *5*, 154.
- [22] M. Kim, J. Fan, *Adv. Fiber Mater.* **2021**, *3*, 160.
- [23] X. Wei, Z. Zhao, C. Zhang, W. Yuan, Z. Wu, J. Wang, Z. L. Wang, *ACS Nano* **2021**, *15*, 13200.

- [24] T. Jiang, L. M. Zhang, X. Chen, C. B. Han, W. Tang, C. Zhang, L. Xu, Z. L. Wang, *ACS Nano* **2015**, *9*, 12562.
- [25] Y. Liu, X. Ou, X. Lei, P. Li, D. Mi, L. Ren, L. Guo, R. Guo, T. Chen, J. Hu, Z. Xiang, *Nat. Commun.* **2020**, *11*, 1620.
- [26] W. He, C. Shan, S. Fu, H. Wu, J. Wang, Q. Mu, G. Li, C. Hu, *Adv. Mater.* **2022**, *35*, 2209657.
- [27] E. C. Shin, J. H. Ko, H. K. Lyeo, Y. H. Kim, *Phys. Rev. Res.* **2022**, *4*, 023131.
- [28] C. A. Mizzi, L. D. Marks, *Nano Lett.* **2022**, *22*, 3939.
- [29] C. A. Mizzi, A. Y. Lin, L. D. Marks, *Phys. Rev. Lett.* **2019**, *123*, 116103.
- [30] A. Šutka, A. Linarts, K. Mälneiks, K. Stiprais, L. Lapčinskis, *Mater. Horiz.* **2020**, *7*, 520.
- [31] M. Sakaguchi, Y. Miwa, S. Hara, Y. Sugino, K. Yamamoto, S. Shimada, *J. Electrost.* **2004**, *62*, 35.
- [32] F. Zhan, A. C. Wang, L. Xu, S. Lin, J. Shao, X. Chen, Z. L. Wang, *ACS Nano* **2020**, *14*, 17565.
- [33] S. Li, J. Nie, Y. Shi, X. Tao, F. Wang, J. Tian, S. Lin, X. Chen, *Adv. Mater.* **2020**, *32*, 2001307.
- [34] A. F. Diaz, R. M. Felix-Navarro, *J. Electrost.* **2004**, *62*, 277.
- [35] D. M. Gooding, G. K. Kaufman, *Encycl. Inorg. Bioinorg. Chem.* **2011**, *1*.
- [36] H. Zou, Y. Zhang, L. Guo, P. Wang, X. He, G. Dai, H. Zheng, C. Chen, A. C. Wang, C. Xu, Z. L. Wang, *Nat. Commun.* **2019**, *10*, 1427.
- [37] P. Zhao, N. Soin, K. Prashanthi, J. Chen, S. Dong, E. Zhou, Z. Zhu, A. A. Narasimulu, C. D. Montemagno, L. Yu, J. Luo, *ACS Appl. Mater. Interfaces* **2018**, *10*, 5880.
- [38] A. R. Nule, B. Dudem, J. S. Yu, *Energy* **2018**, *165*, 677.
- [39] G. Fatti, M. C. Righi, D. Dini, A. Ciniero, *ACS Appl. Polym. Mater.* **2020**, *2*, 5129.
- [40] A. Ciniero, G. Fatti, M. Marsili, D. Dini, M. C. Righi, *Nano Energy* **2023**, *112*, 108502.
- [41] W. Melitz, J. Shen, A. C. Kummel, S. Lee, *Surf. Sci. Rep.* **2021**, *66*, 1.
- [42] M. Nonnenmacher, M. P. O'Boyle, H. K. Wickramasinghe, *Appl. Phys. Lett.* **1991**, *58*, 2921.
- [43] H. Ko, Y. W. Lim, S. Han, C. K. Jeong, S. B. Cho, *ACS Energy Lett.* **2021**, *6*, 2792.
- [44] A. Patra, J. E. Bates, J. Sun, J. P. Perdew, *Proc. Natl. Acad. Sci. U. S. A.* **2017**, *114*, E9188.
- [45] M. Yortanli, E. Mete, *J. Chem. Phys.* **2019**, *151*, 214701.
- [46] H. B. Michaelson, *J. Appl. Phys.* **1977**, *48*, 4729.
- [47] E. Sanville, S. D. Kenny, R. Smith, G. Henkelman, *J. Comput. Chem.* **2007**, *28*, 899.
- [48] W. Tang, E. Sanville, G. Henkelman, *J. Phys.: Condens. Matter* **2009**, *21*, 084204.
- [49] P. C. Rusu, G. Brocks, *J. Phys. Chem. B* **2006**, *110*, 22628.
- [50] G. Fatti, P. Restuccia, C. Calandra, M. C. Righi, *J. Phys. Chem. C* **2018**, *122*, 28105.
- [51] A. Michaelides, P. Hu, M. H. Lee, A. Alavi, D. A. King, *Phys. Rev. Lett.* **2003**, *90*, 246103.
- [52] T. C. Leung, C. L. Kao, W. S. Su, Y. J. Feng, C. T. Chan, *Phys. Rev. B* **2003**, *68*, 195408.
- [53] A. J. Wagner, K. Han, A. L. Vaught, D. H. Fairbrother, *J. Phys. Chem. B* **2000**, *104*, 3291.
- [54] S. Tasker, R. D. Chambers, J. P. S. Badyal, *J. Phys. Chem.* **1994**, *98*, 12442.
- [55] Y. Yamada, E. Mete, *Electrochim. Solid-State Lett.* **2002**, *5*, A283.
- [56] A. Vesel, D. Lojen, R. Zaplotnik, G. Primc, M. Mozetic, J. Ekar, J. Kovac, M. Gorjanc, M. Kurecic, K. Stana-Kleinschek, *Polymers* **2020**, *12*, 2855.
- [57] Z. Li, L. Szlufarska, *Phys. Rev. Lett.* **2021**, *126*, 076001.
- [58] N. N. Gosvami, J. A. Bares, F. Mangolini, A. R. Konicek, D. G. Yablon, R. W. Carpick, *Science* **2015**, *348*, 102.
- [59] L.-T. Li, X. M. Liang, Y. Z. Xing, D. Yan, G. F. Wang, *J. Tribol.* **2021**, *143*, 071501.
- [60] C. X. Lu, C. B. Han, G. Q. Gu, J. Chen, Z. W. Yang, T. Jiang, C. He, Z. L. Wang, *Adv. Energy Mater.* **2017**, *19*, 1700275.
- [61] J.-H. Yang, Y.-K. Kim, J. Y. Lee, *Energies* **2015**, *8*, 12729.
- [62] S. Cho, S. Jang, M. La, Y. Yun, T. Yu, S. J. Park, D. Choi, *Materials* **2020**, *13*, 872.
- [63] J. Luo, Z. L. Wang, *EcoMat* **2020**, *2*, e12059.
- [64] Y. Ra, J. H. Choi, S.-J. Choi, M. La, S. J. Park, M.-J. Kim, D. Choi, *Extreme Mech. Lett.* **2020**, *40*, 100910.
- [65] T. Jing, B. Xu, Y. Yang, C. Jiang, M. Wu, *Nano Energy* **2020**, *78*, 105374.
- [66] C.-Y. Chao, G. L. Jay, *Appl. Phys. Lett.* **2004**, *84*, 2479.
- [67] I. R. G. Ogilvie, V. J. Sieben, C. F. A. Floquet, R. Zmijan, M. C. Mowlem, H. Morgan, *J. Micromech. Microeng.* **2010**, *20*, 065016.
- [68] Z. Lin, J. Chen, J. Yang, *J. Nanomater.* **2016**, *2016*, 5651613.
- [69] P. Giannozzi, S. Baroni, N. Bonini, M. Calandra, R. Car, C. Cavazzoni, D. Ceresoli, G. L. Chiarotti, M. Cococcioni, I. Dabo, A. D. Corso, S. de Gironcoli, S. Fabris, G. Fratesi, R. Gebauer, U. Gerstmann, C. Gougoussis, A. Kokalj, M. Lazzeri, L. Martin-Samos, N. Marzari, F. Mauri, R. Mazzarello, S. Paolini, A. Pasquarello, L. Paulatto, C. Sbraccia, S. Scandolo, G. Sclauzero, A. P. Seitsonen, et al., *J. Phys.: Condens. Matter* **2009**, *21*, 395502.
- [70] J. P. Perdew, K. Burke, M. Ernzerhof, *Phys. Rev. Lett.* **1996**, *77*, 3865.
- [71] S. Grimme, *J. Comput. Chem.* **2006**, *7*, 1787.
- [72] B. N. Dutta, B. Dayal, *Phys. Status Solidi B* **1963**, *3*, 473.
- [73] M. D'Amore, G. Talarico, V. Barone, *J. Am. Chem. Soc.* **2006**, *128*, 1099.
- [74] H. J. Monkhorst, J. D. Pack, *Phys. Rev. B* **1976**, *13*, 5188.
- [75] COMSOL Multiphysics, *Introduction to COMSOL Multiphysics*, COMSOL Multiphysics, Burlington, MA **1998**.
- [76] W. Akram, A. F. Rafique, N. Maqsood, A. Khan, S. Badshah, R. U. Khan, *Materials* **2020**, *12*, 388.
- [77] A. Sharma, M. Untch, J. S. Quinton, R. Berger, G. Andersson, D. A. Lewis, *Appl. Surf. Sci.* **2016**, *363*, 516.
- [78] J. J. Kopanski, M. Y. Afridi, S. Jeliazkov, W. Jiang, T. R. Walker, *AIP Conf. Proc.* **2007**, *931*, 530.
- [79] C. Kim, B. Lee, H. J. Yang, H. M. Lee, J. G. Lee, H. Shin, *J. Korean Phys. Soc.* **2007**, *47*, 417.